

# Activity and Selectivity Control in CO<sub>2</sub> Electroreduction to Multicarbon Products over CuO<sub>x</sub> Catalysts via Electrolyte Design

Dunfeng Gao,<sup>†,‡,§</sup> Ian T. McCrum,<sup>§</sup> Shyam Deo,<sup>§</sup> Yong-Wook Choi,<sup>†,‡</sup> Fabian Scholten,<sup>†,‡</sup> Weiming Wan,<sup>||</sup> Jingguang G. Chen,<sup>||,⊥</sup> Michael J. Janik,<sup>\*,§</sup> and Beatriz Roldan Cuenya<sup>\*,†,‡,§</sup>

<sup>†</sup>Department of Interface Science, Fritz-Haber Institute of the Max Planck Society, 14195 Berlin, Germany

<sup>‡</sup>Department of Physics, Ruhr-University Bochum, 44780 Bochum, Germany

<sup>§</sup>Department of Chemical Engineering, The Pennsylvania State University, 51 Greenberg, University Park, Pennsylvania 16802, United States

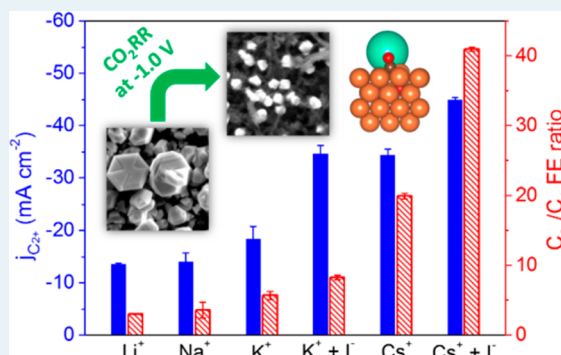
<sup>||</sup>Department of Chemical Engineering, Columbia University, New York, New York 10027, United States

<sup>⊥</sup>Chemistry Department, Brookhaven National Laboratory, Upton, New York 11973, United States

## Supporting Information

**ABSTRACT:** The CO<sub>2</sub> electroreduction reaction (CO<sub>2</sub>RR) to chemicals and fuels is of both fundamental and practical significance, since it would lead to a more efficient storage of renewable energy while closing the carbon cycle. Here we report enhanced activity and selectivity for the CO<sub>2</sub>RR to multicarbon hydrocarbons and alcohols (~69% Faradaic efficiency and -45.5 mA cm<sup>-2</sup> partial current density for C<sub>2+</sub> at -1.0 V vs RHE) over O<sub>2</sub>-plasma-activated Cu catalysts via electrolyte design. Increasing the size of the alkali-metal cations in the electrolyte, in combination with the presence of subsurface oxygen species which favor their adsorption, significantly improved C–C coupling on CuO<sub>x</sub> electrodes. The coexistence of Cs<sup>+</sup> and I<sup>-</sup> induced drastic restructuring of the CuO<sub>x</sub> surface, the formation of shaped particles containing stable CuI species, and a more favorable stabilization of the reaction intermediates and concomitant high C<sub>2+</sub> selectivity. This work, combining both experiment and density functional theory, provides insights into the active sites and reaction mechanism of oxide-derived Cu catalysts for the CO<sub>2</sub>RR.

**KEYWORDS:** CO<sub>2</sub> electroreduction, CuO<sub>x</sub> catalysts, electrolyte design, cation adsorption, subsurface oxygen



## 1. INTRODUCTION

The production of chemicals and fuels from the electroreduction of CO<sub>2</sub> (CO<sub>2</sub>RR) has attracted great attention, since it can help to close the anthropogenic carbon cycle and contribute to a more efficient storage of renewable energy.<sup>1–3</sup> In particular, the generation of multicarbon alcohol and hydrocarbon products (C<sub>2+</sub>) over Cu catalysts is highly desirable in order to access liquid fuels and chemicals with high energy density.<sup>4–6</sup> In order to overcome the high overpotential, low C<sub>2+</sub> selectivity, and poor stability of polycrystalline Cu,<sup>7,8</sup> various catalyst design and preparation strategies, including nanostructuring, oxidation pretreatments, and the synthesis of size- and shape-controlled nanoparticles (NPs), modifying Cu with a second component, have been employed.<sup>9–28</sup>

Apart from the structure and electronic properties of the catalysts, the activity and selectivity are also closely related to the composition and nature of the electrolyte. Bicarbonate can facilitate the CO<sub>2</sub>RR by increasing the CO<sub>2</sub> concentration near the electrode surface through a rapid equilibrium with dissolved CO<sub>2</sub>.<sup>29,30</sup> Adding halides to the bicarbonate electro-

lyte may further improve the CO<sub>2</sub>RR by facilitating the stabilization of the carboxyl intermediate.<sup>31–33</sup> Electrolytes containing larger alkali-metal cations resulted in improved C<sub>2+</sub> formation on metallic Cu foils as well as on Cu(100) and Cu(111) surfaces.<sup>34–36</sup> The dependence of the product distribution on the cation type was attributed to a distinct specific adsorption, preferential hydrolysis, or an electrostatic interaction between solvated cations and adsorbed species in the outer Helmholtz plane (OHP).<sup>34–37</sup>

Plasma-activated Cu catalysts have shown vastly improved activity and C<sub>2+</sub> selectivity, due to their enhanced roughness and the presence of subsurface oxygen and Cu<sup>+</sup> species during the reaction.<sup>13,16</sup> In comparison to a metallic Cu catalyst, O<sub>2</sub>-plasma-oxidized Cu catalysts were found to be much more sensitive to the electrolyte composition, such as the presence of halides.<sup>31,32</sup> In this work we investigate the synergistic effect of alkali-metal cations and halide ions on the CO<sub>2</sub>RR to

Received: July 3, 2018

Revised: August 9, 2018

Published: September 11, 2018

multicarbon products over plasma-oxidized Cu catalysts. It has been observed that increasing the cation size significantly improved the activity and  $C_{2+}$  selectivity. Density functional theory (DFT) calculations indicate that the more favorable adsorption of larger cations on  $CuO_x$  results in the stabilization of  $CO_2RR$  intermediates leading to  $C_{2+}$  formation. The  $C_{2+}$  production was further increased by adding  $I^-$  to the  $CsHCO_3$  solution, probably due to a significant surface restructuring, improved stability of  $Cu^+$  species under reaction conditions, and stronger binding of CO.

## 2. RESULTS AND DISCUSSION

**2.1. Electrolyte-Driven Nanostructuring.** Plasma-activated Cu catalysts were synthesized by treating an electropolished Cu foil (EP) with low-pressure  $O_2$  plasma.<sup>13</sup> Figure 1

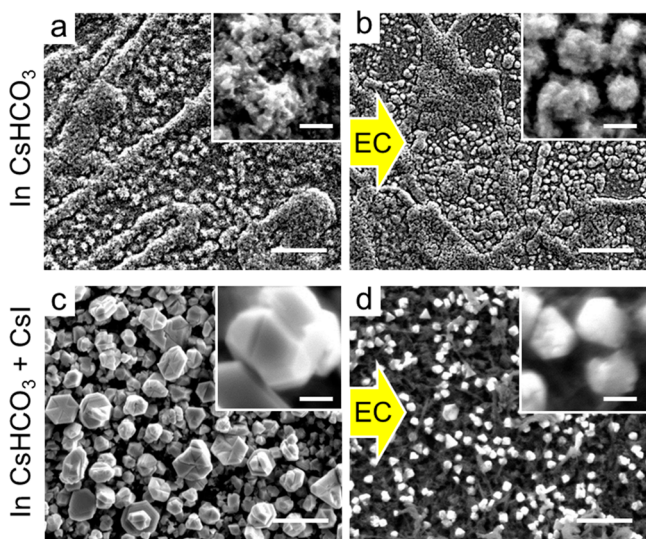


**Figure 1.** SEM images acquired on O2P2 samples after 30 min immersion in (a) 0.1 M  $CsHCO_3$  (O2P2-Cs) and (c) 0.1 M  $CsHCO_3$  + 0.1 M  $CsI$  (O2P2-CsI) solutions. Images acquired after 1 h of  $CO_2RR$  at  $-1.0$  V vs RHE are also shown (b, d). The scale bars in the main images and inserts are  $5\ \mu m$  and  $500\ nm$ , respectively.

and Figure S1 show scanning electron microscope (SEM) images acquired on  $O_2$ -plasma-treated Cu foils (O2P2, 20 W, 2 min) after 30 min immersion (without an applied potential) and after 1 h of the  $CO_2RR$  at  $-1.0$  V vs RHE in the corresponding electrolytes (see sample preparation conditions and electrolyte description in Table S1). The different cations did not obviously change the morphology of the  $CuO_x$  foils (O2P2-Li, Na, K, Cs) both before and after the  $CO_2RR$ , as well as the amount of oxygen (4–5 atom %) detected by energy-dispersive X-ray spectroscopy (EDX) after the  $CO_2RR$  (Table S2). However, the presence of  $CsI$  induced the formation of  $Cu_xO_yI_z$  ( $x:y:z = 46:12:42$  atom %) crystals with sizes of 1–3  $\mu m$  even at open circuit potential. After the  $CO_2RR$ , shaped  $Cu_xO_yI_z$  ( $x:y:z = 67:6:27$  atom %) particles with sizes of 0.5–0.8  $\mu m$  were still present on the surface of O2P2-CsI, surrounded by other rough regions mainly composed of metallic Cu. This is in clear contrast with our previous findings on samples exclusively treated in KI (O2P2-KI),<sup>31</sup> where shaped particles were not observed after the reaction (Figure S1i). The latter suggests that  $Cs^+$  is able to stabilize  $CuI$  species at very negative potentials, which could lead to more  $Cu^+$  species during the reaction.

In order to understand the binding thermodynamics of the key intermediate CO, temperature-programmed desorption (TPD) of CO was conducted. The  $O_2$ -plasma treatment conditions strongly affected the surface structure, density, and type of defects in the pristine  $O_2$ -plasma-activated Cu samples (Figure 2a). Apart from the low-temperature desorption

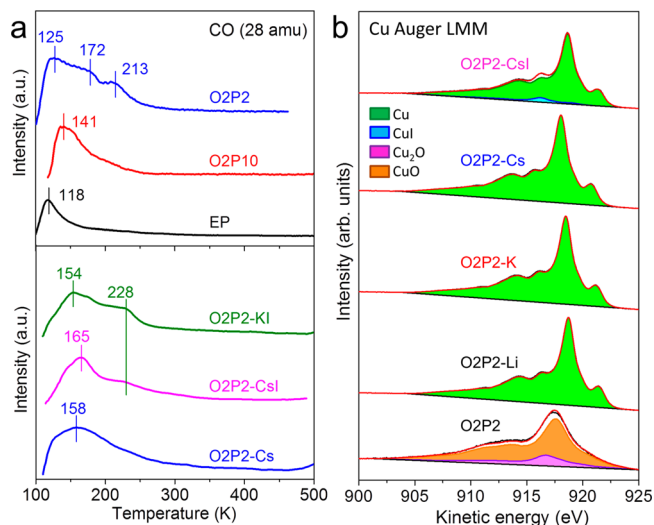


**Figure 2.** (a) CO TPD profiles of (top) pristine  $O_2$ -plasma-activated (20 W 2 min (O2P2) and 100 W 10 min (O2P10)) Cu foils as well as an electropolished (EP) Cu foil and (bottom) O2P2 pretreated in different electrolytes containing KI, CsI and Cs. (b) Quasi in situ Cu Auger LMM spectra of O2P2 after 1 h of  $CO_2RR$  at  $-1.0$  V vs RHE in different electrolytes containing CsI, Cs, K, and Li, as well as the pristine O2P2.

feature at 125 K, O2P2 showed two CO desorption features at 172 and 213 K, corresponding to binding energies of 10.8 and 13.5  $kcal\ mol^{-1}$  following a first-order Redhead model.<sup>38</sup> In comparison to the  $O_2$  100 W 10 min plasma treated Cu foil (O2P10) and the electropolished Cu foil (EP), the presence of stronger CO binding sites on O2P2, such as defects or low-coordinated sites at stepped facets, is evident.<sup>12</sup> Remarkably, the dependence of the CO binding energy on the  $O_2$ -plasma treatment conditions directly correlated with the ethylene selectivity.<sup>13</sup> The CO-binding sites on O2P2 were also investigated before the  $CO_2RR$  after a sample pretreatment in different electrolytes (Figure 2b). Although the strongest CO-binding sites observed in the clean O2P2 sample were lost in O2P2-Cs (missing peaks at 172 and 213 K), such sites are recovered upon subsequent sample restructuring with  $I^-$  (228 K peak for O2P2-KI and O2P2-CsI). This reveals that the shaped-Cu crystals formed on the latter samples act as strong CO-binding sites.

Quasi in situ X-ray photoelectron spectroscopy (XPS) is an efficient surface-sensitive technique to detect the oxidation state of electrocatalysts at different reaction stages without exposure to air.<sup>31</sup> Consistent with EDX measurements, the surface of the as-prepared O2P2 sample was composed of a mixture of  $Cu_2O$  and  $CuO$ . After the reaction,  $CuO_x$  in the O2P2 sample was mostly reduced, with only metallic Cu detected on the surface of samples O2P2-Li, O2P2-Na, O2P2-K, O2P2-Cs, and  $\sim 8\%$   $Cu^+$  species on O2P2-CsI. By analyzing the I-3d and O-1s spectra (Figure S2), we confirmed that most of the  $Cu^+$  species detected after the  $CO_2RR$  exist in the form of  $CuI$ . The surface  $Cu^+$  species resistant to reduction under

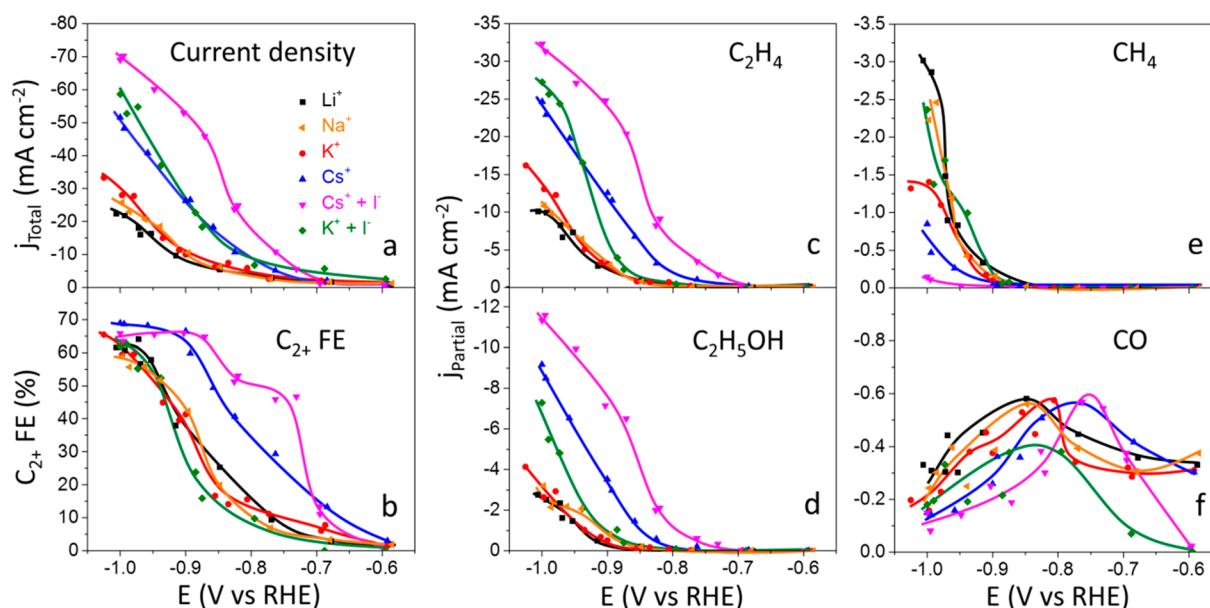


**Figure 3.** (a) Geometric current densities, (b) total FEs of  $\text{C}_{2+}$  products, and partial current densities of (c)  $\text{C}_2\text{H}_4$ , (d)  $\text{C}_2\text{H}_5\text{OH}$ , (e)  $\text{CH}_4$ , and (f)  $\text{CO}$  as a function of applied potential for sample O2P2 measured in different electrolytes after 1 h of  $\text{CO}_2\text{RR}$ . Solid lines are guides for the eye.

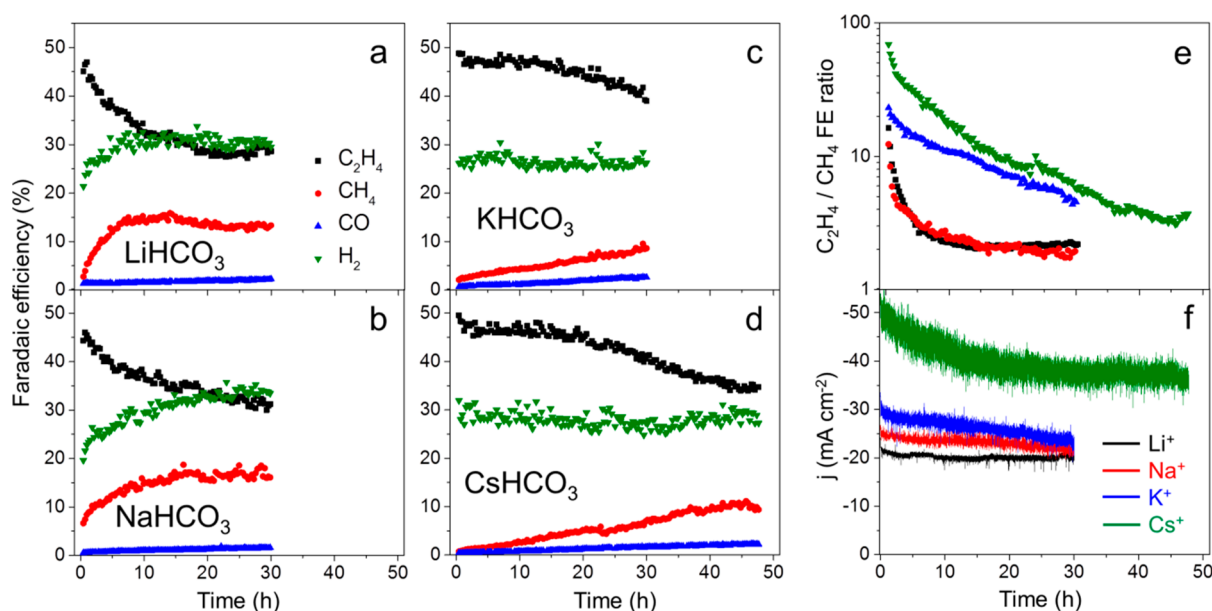


**Figure 4.** Time-dependent FEs of major gas products at  $-1.0$  V vs RHE in  $0.1$  M  $\text{LiHCO}_3$  (a),  $0.1$  M  $\text{NaHCO}_3$  (b),  $0.1$  M  $\text{KHCO}_3$  (c), and  $0.1$  M  $\text{CsHCO}_3$  (d) solutions. Time-dependent FE ratios of ethylene/methane (e) and current densities (f) in (a)–(d).

$\text{CO}_2\text{RR}$  potentials could be stabilized by the adsorbed iodine ions as well as the subsurface oxygen and  $\text{Cu}^+$  species<sup>13,39–43</sup> in the oxide-derived Cu catalysts.

**2.2.  $\text{CO}_2$  Electroreduction Performance.** The current densities over  $\text{O}_2$ -plasma-activated Cu showed a strong dependence on the alkali-metal cation size in the order  $\text{Li}^+ < \text{Na}^+ < \text{K}^+ < \text{Cs}^+$  (Figure 3a) and are much higher than those obtained for electropolished metallic Cu.<sup>34</sup> The increased activity on oxidized Cu foils over metallic foils was previously attributed to the increased roughness, defects, and the presence of  $\text{Cu}^+$  species or subsurface oxygen species.<sup>12,13,16,39,42,44–46</sup> Double-layer capacitance measurements (Figure S3) indicated similar roughness of the samples after treatments in distinct  $\text{MHCO}_3$ . The activity reported was further corroborated when current densities normalized by the electrochemical surface

area (ECSA) were considered<sup>12</sup> (Figure S4). Therefore, the activity difference is not caused by a structural change of the catalysts, but by a chemical effect derived from the nature of the cations. We further optimized the electrolyte by using  $0.1$  M  $\text{CsHCO}_3 + 0.1$  M  $\text{CsI}$ . The presence of  $\text{I}^-$  significantly increased the current density, mainly attributed to the strong specific adsorption of  $\text{I}^-$  and the concomitant increased roughness.<sup>31,47</sup> Moreover, a higher content of  $\text{Cu}^+$  was stabilized during the  $\text{CO}_2\text{RR}$  due to the  $\text{I}^-$ -induced Cu nanostructuring. The increased current density in the presence of  $\text{Cs}^+ + \text{I}^-$  over  $\text{K}^+ + \text{I}^-$  further verified the stronger promoting effect of larger cations on the  $\text{CO}_2\text{RR}$ .

Figure 3b, Figure S5 and Figure S6 show the potential-dependent Faradaic efficiencies (FEs) of  $\text{CO}_2\text{RR}$  products. Higher  $\text{C}_{2+}$  FEs ( $\sim 69\%$  on O2P2-Cs at  $-1.0$  V vs RHE, Figure



3b) were observed in the presence of  $\text{Cs}^+$ , especially on the O2P2-CsI sample at lower overpotentials (see also the  $\text{C}_{2+}/\text{C}_1$  FE ratio in Figure S7). With an increase in the cation size, the partial current densities of  $\text{C}_{2+}$  products were remarkably increased, while the formation of methane and CO was significantly suppressed (Figure 3c–f and Figure S8), demonstrating that larger cations facilitate C–C coupling versus  $\text{C}_1$  pathways (CO desorption or further hydrogenation to methane). The additionally increased  $\text{C}_{2+}$  production when  $\text{Cs}^+$  and  $\text{I}^-$  were both present in the electrolyte is likely related to the observed stabilization of shaped particles with a high amount of  $\text{Cu}^+$  species and to the stronger CO binding sites available on the  $\text{CuO}_x$  foil after  $\text{Cs}^+$  +  $\text{I}^-$  exposure, which have been shown to facilitate C–C coupling (Figure S9).<sup>12</sup> With increasing cation size and the presence of  $\text{I}^-$ , the competitive  $\text{H}_2$  partial current density was also found to increase, while the  $\text{H}_2$  FE did not obviously change at more negative potentials and seemed to be independent of the cation size. Therefore, the cation effect on the competitive hydrogen evolution reaction observed here for  $\text{CuO}_x$  catalysts was different from that observed on metallic Cu.<sup>34,36</sup> Our  $\text{O}_2$ -plasma-activated Cu catalyst, with both high  $\text{C}_{2+}$  FE and high partial current density ( $-45.5 \text{ mA cm}^{-2}$  on O2P2-CsI, Figure S10), exhibits superior ability for  $\text{C}_{2+}$  production in comparison to previously reported catalysts (Table S3).

**2.3. Effect of Cations on the Stability.** The effect of alkali-metal cations on the stability of the  $\text{O}_2$ -plasma-activated Cu catalysts during the  $\text{CO}_2$ RR was studied at  $-1.0 \text{ V}$  vs RHE in  $0.1 \text{ M}$   $\text{MHCO}_3$  solutions, as shown in Figure 4. The ethylene FE of O2P2-Li drastically decreased to  $\sim 35\%$  while the methane FE increased to  $\sim 14\%$  in the first 7 h. A similar trend was also observed on O2P2-Na. However, the deactivation became much slower on O2P2-K and O2P2-Cs. The ethylene FEs of both O2P2-K and O2P2-Cs were nearly stable ( $>45\%$ ) in the first 20 h, while the methane FE slightly increased to  $\sim 6\%$  on O2P2-K and O2P2-Cs. The long-term stability tests indicated the superior effect of larger cations on the stable  $\text{C}_{2+}$  formation. The slow time-dependent decrease in current density and ethylene/methane FE ratio in all electrolytes are not dominated by the nature of the cations but are likely due to the sluggish removal of subsurface oxygen species at very negative potentials for  $\text{CO}_2$  reduction as well as to the gradual decrease in the roughness of the sample (roughness factor 24.7 after 1 h versus 11.5 after 30 h in  $0.1 \text{ M}$   $\text{KHCO}_3$ ) and associated decrease in the content of strong CO-binding sites in the course of the reaction.

**2.4. C–C Coupling Tuned by Specific Cation Adsorption.** DFT calculations were used to examine the specific adsorption of Li, Na, K, and Cs onto Cu(111), Cu(100), and Cu(211) at low ( $1/9 \text{ ML}$ ) coverage (Figure 5a). The near-surface region was solvated with  $6\text{H}_2\text{O}^*$  on all three surfaces (forming a water bilayer) to approximate the solvent near the electrode surface (Figure S11). All cations adsorb favorably on Cu(111) and Cu(100) below  $-1 \text{ V}_{\text{NHE}}$  and on Cu(211) below  $-1.5 \text{ V}_{\text{NHE}}$ ; therefore, specific adsorption is favorable at moderate  $\text{CO}_2$ RR overpotentials. As the alkali-metal cations retain most of their charge on adsorption, the presence of near-surface solvation significantly promotes adsorption (Figure S12). We examined the interaction between the adsorbed cations and reaction intermediates by considering  $\text{CO}^*$ ,  $\text{OCCO}^*$ , and  $\text{OCCOH}^*$  intermediates which dictate  $\text{C}_{2+}$  formation on Cu(100).<sup>48</sup> We have focused on Cu(100), as it has been shown experimentally to be the

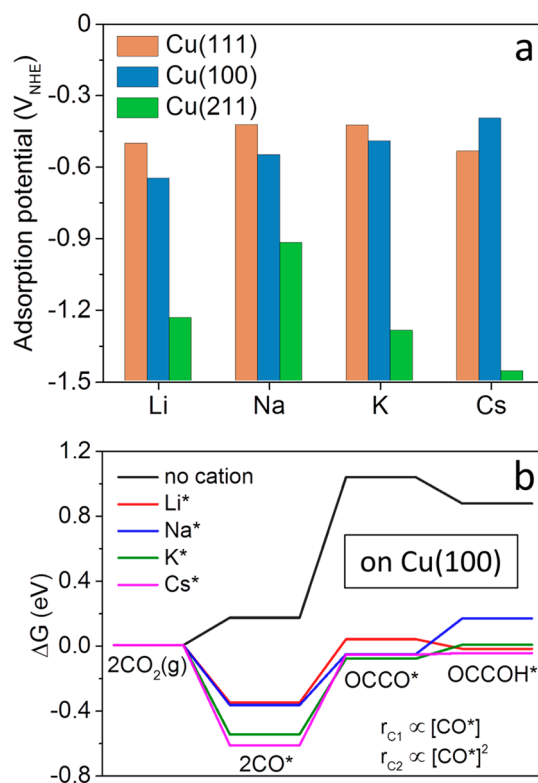


**Figure 5.** (a) Equilibrium adsorption potential of Li, Na, K, and Cs at  $1/9 \text{ ML}$  on Cu(111), Cu(100), and Cu(211). Adsorption is calculated from a  $1 \text{ M}$  solution of the alkali-metal cations at  $300 \text{ K}$ . The near-surface region is solvated with  $6 \text{ H}_2\text{O}^*$ . (b) Formation free energy of  $\text{CO}^*$ ,  $\text{OCCO}^*$ , and  $\text{OCCOH}^*$  relative to  $\text{CO}_2(\text{g})$ ,  $\text{H}_2(\text{g})$ , and  $\text{H}_2\text{O}(\text{aq})$  at  $1/9 \text{ ML}$  on Cu(100) at  $300 \text{ K}$ . Energies relative to  $\text{H}_2(\text{g})$  are equivalent to giving the energy relative to protons and electrons at an electrode potential of  $0 \text{ V}$  on an RHE scale. The formation energy is calculated in the absence and the presence of  $\text{Li}^+$ ,  $\text{Na}^+$ ,  $\text{K}^+$ , and  $\text{Cs}^+$  at  $1/9 \text{ ML}$ .

most active low-index facet for  $\text{C}_{2+}$  formation and may dominate the measured selectivity.<sup>49–52</sup> Figure 4b shows that all the cations promote the formation of  $\text{CO}^*$ ,  $\text{OCCO}^*$ , and  $\text{OCCOH}^*$ . The presence of a near-surface electric field, due to either artificial application or the presence of solvated alkali-metal cations in the OHP<sup>36</sup> or adsorbed on the surface,<sup>35,48</sup> promotes the formation of polar or highly polarizable intermediates. The formation rate of  $\text{C}_2$  products is proportional to the  $\text{CO}^*$  coverage squared, while the  $\text{C}_1$  formation rate is only linearly proportional to the  $\text{CO}^*$  coverage. Therefore, we expect that the promotion of  $\text{CO}^*$  adsorption would lead to greater C–C coupling and higher  $\text{C}_{2+}$  selectivity, further accentuated by promotion of the adsorption strength of the  $\text{OCCO}^*$  and  $\text{OCCOH}^*$  intermediates.

In contrast to what others have found previously with cations only populating the OHP,<sup>36</sup> we find that the effect of the specifically adsorbed cations on the formation of  $\text{CO}^*$ ,  $\text{OCCO}^*$ , and  $\text{OCCOH}^*$  is dependent on the cation identity. This may be due to their closer position to these intermediates when the cations are adsorbed on the surface (average ion–surface distance:  $3.6 \text{ \AA}$  on Cu(100) with  $6\text{H}_2\text{O}^*$ ), relative to only occupying the OHP (average ion–surface distance:  $5.1 \text{ \AA}$  on Cu(111)).<sup>36</sup> The magnitude of the interaction between these cations and the intermediates correlates with the surface normal dipole moment generated on cation-specific adsorption (Figure S13), with adsorbed Cs generating the strongest dipole

moment and largest interaction with  $\text{CO}^*$ ,  $\text{OCCO}^*$ , and  $\text{OCCOH}^*$ . This matches the experimental trend in the  $\text{C}_{2+}$  formation, where the more favorable  $\text{CO}^*$  formation in the presence of  $\text{Cs}^+$  results in a higher  $\text{C}_{2+}$  production rate in the Cs-containing electrolyte at lower overpotentials. Further, the adsorption strength of the cations follows the trend  $\text{Li} < \text{Na} < \text{K} < \text{Cs}$  on  $\text{Cu}(100)$ , with Cs giving the most favorable adsorption.

The effect of the alkali-metal cations on the formation of the intermediates (Figure 5b) was calculated in the absence of near-surface solvation, which we expect to weaken the interaction between the cations and intermediates but maintain the trend among the cations. Our prior work showed that the presence of alkali-metal cations near the electrode surface increased the activation barrier for  $\text{CO}_2$  reduction steps which involved the shuttling of protons through water near the electrode surface,<sup>47</sup> which could hinder formation of  $\text{C}_1$  over  $\text{C}_{2+}$ . Further, while we have limited our focus to the effect of the cations on  $\text{CO}^*$ ,  $\text{OCCO}^*$ , and  $\text{OCCOH}^*$ , the alkali-metal cations, once near the electrode surface, may affect many important intermediates present in the path to  $\text{C}_1$  and  $\text{C}_{2+}$  products, as well as activation barriers between these reaction intermediates (beyond just proton transfer). Therefore, our intent is to only highlight that the cations have an effect on the binding strength of these important intermediates and that the trend in the effect on  $\text{CO}^*$  adsorption matches the trend in the generation of  $\text{C}_{2+}$  products.  $\text{CO}^*$  is an important intermediate not only because it is common to both the  $\text{C}_1$  and  $\text{C}_{2+}$  paths but also because it is a useful descriptor in understanding the binding strength of all carbon-containing species which adsorb to the surface through a carbon atom, as their formation energies are known to scale linearly with that of  $\text{CO}^*$ , following a scaling relation.<sup>53,54</sup> Future work should examine the effect of alkali-metal cations on the binding strength of all possible intermediates, as well as on the activation barriers for C–C coupling.

**2.5. Role of Subsurface Oxygen.** DFT calculations were also used to examine the effects of subsurface oxygen present in the copper electrode after plasma-oxidation pretreatment. Figure 6a shows that subsurface oxygen at 2/9 ML (and the generated  $\text{Cu}^+$  species at the electrode surface) promotes the adsorption of the alkali-metal cations to  $\text{Cu}(100)$  by 0.1–0.3 eV. The promotion of cation adsorption by subsurface oxygen would increase the cation coverage at any given potential. Figure 6b shows that the presence of subsurface oxygen also accentuates the effect of the cations, significantly promoting  $\text{CO}^*$  formation, beyond that seen for the cations alone (Figure 5b), with  $\text{Cs}^+$  promoting  $\text{CO}^*$  formation the most (by 0.65 eV relative to  $\text{CO}^*$  formation on the bare, non-oxidized, cation-free  $\text{Cu}(100)$  surface). These results provide an indication that subsurface oxygen species can further promote  $\text{C}_{2+}$  formation. While the particular subsurface oxygen model we used was thermodynamically unstable relative to reduction to form water at  $\text{CO}_2\text{RR}$  potentials, we find that an oxygen-driven reconstruction of  $\text{Cu}(100)$  also promotes cation adsorption, even in the absence of surface or subsurface oxygen (Figure S14).<sup>55</sup>

In a recent study, increasing cation size resulted in an increase in the formation of ethylene and ethanol on metallic Cu, with little to no effect on the formation of CO and methane.<sup>36</sup> In contrast, on our  $\text{CuO}_x$  samples, the increased  $\text{C}_{2+}$  formation correlates with a decrease in the production of CO and methane (Figure 3), suggesting a preferred formation

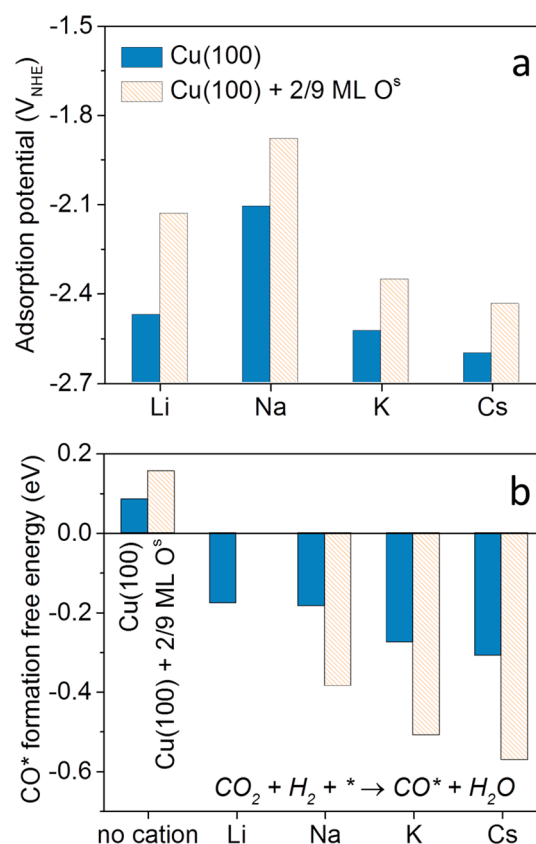


**Figure 6.** (a) Equilibrium adsorption potential of Li, Na, K, and Cs at 1/9 ML on  $\text{Cu}(100)$  in the absence and presence of subsurface oxygen (2/9 ML  $\text{O}^s$ ). (b)  $\text{CO}^*$  formation free energy calculated in the absence and presence of  $\text{Li}^+$ ,  $\text{Na}^+$ ,  $\text{K}^+$ , and  $\text{Cs}^+$  on bare  $\text{Cu}(100)$  and  $\text{Cu}(100)$  with 2/9 ML  $\text{O}^s$ . As subsurface oxygen migrated to the surface in the presence of coadsorbed  $\text{Li}^+$  and  $\text{CO}^*$ , this data point has been excluded from (b).

of  $\text{C}_{2+}$  over  $\text{C}_1$ . The difference in the  $\text{C}_1$  formation is mainly related to the subsurface oxygen and  $\text{Cu}^+$  species in the  $\text{CuO}_x$  as supported by DFT calculations, as well as the presence of a possible interface between the  $\text{Cu}^+$  and adjacent  $\text{Cu}^0$ , which could also promote C–C coupling.<sup>39,45,56–59</sup>

**2.6. Effect of Adsorbed Iodide.** We previously found that iodide remains specifically adsorbed on Cu at small applied overpotentials during the  $\text{CO}_2\text{RR}$  and affects the binding of various  $\text{CO}_2\text{RR}$  intermediates. Here we examined theoretically the effect of specifically adsorbed iodide on alkali-metal cation adsorption in the presence of 6  $\text{H}_2\text{O}^*$ . While there is a small effect, in particular, a weakening of the binding of the larger cations (K, Cs) (Figure S15), the complexity of possible interactions among coadsorbed cation, iodide, and reaction intermediates leaves DFT studies of the collective effects involving iodide (particularly in the presence of Cs) as future work. See additional discussion in the Supporting Information.

### 3. CONCLUSIONS

In summary, increasing the alkali-metal cation size significantly improved  $\text{C}_{2+}$  production, with the highest FE of ~69%. The  $\text{C}_{2+}$  formation was further increased by adding  $\text{I}^-$  to the  $\text{CsHCO}_3$  solution ( $-45.5 \text{ mA cm}^{-2}$   $\text{C}_{2+}$  partial current density), likely due to the presence of shaped particles with a high amount of  $\text{Cu}^+$  species during the reaction. DFT calculations show that the specific adsorption of the alkali-

metal cations is favorable during the CO<sub>2</sub>RR and that the presence of the adsorbed cations promotes the formation of CO<sub>2</sub>RR intermediates (CO\*, OCCO\*, OCCOH\*) that lead to C<sub>2+</sub> products. The promoting effect is cation specific, with cesium showing the largest promoting effect, consistent with our experimental observation. Our preliminary DFT results indicate that subsurface oxygen, Cu<sup>+</sup> species, and a surface reconstruction introduced by the plasma-oxidation pretreatment lead to a promotion of alkali-metal cation adsorption onto Cu surfaces and that subsurface oxygen accentuates the promoting effects of the alkali cations on CO\* formation.

## 4. EXPERIMENTAL AND THEORETICAL METHODS

**4.1. Catalyst Synthesis.** Commercial Cu foils (Advent Research Materials Ltd., 99.995%) were first cleaned with acetone and ultrapure water (18.2 MΩ) in an ultrasonic bath and then electropolished in phosphoric acid (VWR, 85 wt %) at 3 V versus a titanium foil for 5 min. The electropolished Cu foil was further treated in a plasma etcher (Plasma Prep III, SPI Supplies) at a gas pressure of 400 mTorr of O<sub>2</sub> for the indicated plasma power and time.<sup>13</sup> The plasma-oxidized Cu foils were pretreated in different electrolytes for further characterization (see Table S1).

**4.2. Scanning Electron Microscopy (SEM) Characterization.** The morphology of the O<sub>2</sub>-plasma-treated Cu foils was investigated by SEM using a Quanta 200 FEG microscope from FEI with a field emitter as the electron source. The images were acquired under vacuum using a secondary electron (Everhart-Thornley) detector. An acceleration voltage of 10 keV was used. A liquid-N<sub>2</sub>-cooled energy-dispersive X-ray spectroscopy (EDX) detector was employed for the elemental analysis of the sample. The error bars in the content of all elements were made on the basis of the EDX spectra from at least six different positions of two identical samples. The samples after the reaction were washed thoroughly with water and transferred immediately to the SEM chamber in order to minimize air exposure. The amount of oxygen resulting from air exposure was negligible and did not affect the elemental analysis results, given that EDX, with a probing depth of ~300 nm at 10 keV, is not surface-sensitive enough.<sup>16</sup>

**4.3. Quasi in Situ X-ray photoelectron Spectroscopy (XPS) Characterization.** The quasi in situ XPS measurements were carried out in an ultrahigh-vacuum (UHV) setup equipped with a nonmonochromatic Al X-ray source ( $h\nu = 1486.6$  eV) and a hemispherical electron analyzer (Phoibos 100, SPECS GmbH). The Cu 2p<sub>3/2</sub> peak corresponding to CuO (933.11 eV)<sup>60</sup> was used for the energy alignment of the as-prepared plasma-oxidized sample. For the rest of the samples which do not contain any Cu<sup>2+</sup> species, the peak corresponding to Cu<sub>2</sub>O (932.67 eV)<sup>60</sup> was used instead. The XPS analysis chamber was connected to an in situ electrochemical (EC) cell (SPECS GmbH). An Autolab potentiostat (PGSTAT 302N) was used for the electrochemical measurements. The sample transfer from the EC cell to the XPS UHV chamber was performed under vacuum. All XPS spectra were acquired at room temperature. For the deconvolution of the Cu LMM Auger spectra, data acquired in our laboratory from a metallic Cu<sup>0</sup> foil (reduced in situ by H<sub>2</sub> plasma), CuI powder from our laboratory, and CuO and Cu<sub>2</sub>O foils from the literature<sup>16</sup> were used as references. The Cu Auger spectra are more sensitive to the presence of Cu<sup>+</sup> species, in particular Cu<sub>x</sub>O, in comparison to the O 1s spectra, because the latter are dominated by the contribution of adsorbed species not

associated with Cu<sup>+</sup>. They also allow us to distinguish Cu<sup>+</sup> from Cu<sup>0</sup>, which is not the case when the Cu 2p XPS region is evaluated.<sup>16</sup>

**4.4. Temperature-Programmed Desorption (TPD) Measurements.** The TPD experiments were performed in a stainless-steel UHV chamber equipped with a quadrupole mass spectrometer (UTI 100C). The Cu foil was placed in the sample holder, which consisted of a tantalum foil (Alfa Aesar, 99.9%), K-type thermocouple, and two tantalum bars (Alfa Aesar, 99.9%). The Cu sample was mounted on a tantalum foil, and a K-type thermocouple was welded to the back of the tantalum foil to measure the temperature of the sample holder. The CO gas was in research purity. The doses were reported in langmuir (1 L = 10<sup>-6</sup> Torr·s) and were uncorrected for ion gauge sensitivity. After the sample was cooled to 100 K, 10 L of CO was dosed into the chamber and CO TPD was carried out with a linear heating rate of 1 K s<sup>-1</sup> from 100 to 500 K.

The binding energy of CO was calculated using the Redhead equation (assuming first-order desorption).<sup>38</sup>

$$\frac{E_a}{RT_p} + \ln\left(\frac{E_a}{RT_p}\right) = \ln\left(\frac{AT_p}{\beta}\right)$$

$A$  is the pre-exponential factor and is assumed to be 10<sup>13</sup>.  $E_a$  is the CO binding energy, and  $R$  is the ideal gas constant.  $\beta$  is the heating rate, and  $T_p$  is the peak temperature of CO desorption. Therefore, the CO binding is correlated with the peak temperature of CO desorption.

**4.5. Electrochemical Measurements.** Electrochemical measurements were carried out in a gas-tight H-cell separated by an anion exchange membrane (Selemion AMV, AGC Inc.). Working electrode and counter electrode compartments were both filled with 40 mL of electrolyte and purged continuously with CO<sub>2</sub> (99.995%, 20 mL min<sup>-1</sup>). The contents of the working electrode compartment were vigorously stirred (1100 rpm). Aqueous 0.1 M LiHCO<sub>3</sub>, 0.1 M NaHCO<sub>3</sub>, 0.1 M KHCO<sub>3</sub> (Honeywell Fluka, 99.7%), 0.1 M CsHCO<sub>3</sub> (Alfa Aesar, 99.99%), 0.1 M CsHCO<sub>3</sub> + 0.1 M CsI (Alfa Aesar, 99.999%), and 0.1 M KHCO<sub>3</sub> + 0.3 M KI (Sigma-Aldrich, 99%) solutions were used as electrolytes (pH 6.8). A 0.1 M LiHCO<sub>3</sub> solution was prepared by saturating 0.05 M Li<sub>2</sub>CO<sub>3</sub> (Sigma-Aldrich, 99.99%) with a flow of pure CO<sub>2</sub> at 1 bar overnight. CsHCO<sub>3</sub> or KHCO<sub>3</sub> was used as a reference and a buffer to avoid significant changes in the pH, which could alter the reaction pathway for ethylene/methane formation.<sup>31</sup> The effect of iodine was studied in 0.1 M CsHCO<sub>3</sub> + 0.1 M CsI or 0.1 M KHCO<sub>3</sub> + 0.3 M KI. All of the electrolytes were prepared with ultrapure water and further prepurified with Chelex 100 Resin (Bio-Rad, 100–200 mesh).<sup>61</sup> The as-received Chelex resin was pretreated before use with 0.5 M H<sub>2</sub>SO<sub>4</sub> (ACS reagent, 95.0–98.0%, Sigma-Aldrich) for 12 h followed by 1 M KOH (99.97%, Sigma-Aldrich) at 60 °C for 24 h, and so the Na<sup>+</sup> ions in the pristine resin were replaced by K<sup>+</sup> ions. In the cases of LiHCO<sub>3</sub> and NaHCO<sub>3</sub>, the pristine resin was used. Prior to the measurement, the electrolyte was bubbled with CO<sub>2</sub> for 30 min to remove oxygen in the solution. A platinum gauze (MaTecK, 3600 mesh cm<sup>-2</sup>) was used as a counter electrode and a leak-free Ag/AgCl/3.4 M KCl electrode (Innovative Instruments, Inc.) as a reference electrode. The O<sub>2</sub>-plasma-treated Cu foil was used as a working electrode. The effective geometric surface area of the Cu foil is 0.5–4 cm<sup>2</sup> depending on the potential investigated. A fresh sample was measured with a chronoamperometric step



for 1 h at each potential, unless stated otherwise. The potentials were controlled with an Autolab potentiostat (PGSTAT 302N). All potentials versus Ag/AgCl were converted to the reversible hydrogen electrode (RHE) scale and corrected for  $iR$  drop as determined by current interrupt. The roughness factors were determined by measuring double-layer capacitance with cyclic voltammetry between 0 and 0.25 V vs RHE, after 1 h of  $\text{CO}_2$  electroreduction in different electrolytes at  $-1.0$  V vs RHE.<sup>16,31</sup> In the case of 0.1 M  $\text{CsHCO}_3$  + 0.1 M CsI and 0.1 M  $\text{KHCO}_3$  + 0.3 M KI, the samples were transferred to 0.1 M  $\text{CsHCO}_3$  and 0.1 M  $\text{KHCO}_3$  for the capacitance measurements after 1 h of  $\text{CO}_2$  electroreduction at  $-1.0$  V vs RHE and thorough washing with water.

**4.6. Product Analysis.** The gas products were analyzed by online gas chromatography (GC, Agilent 7890A). Carboxylates (formate and acetate) were analyzed by high-performance liquid chromatography (HPLC, Shimadzu Prominence), while alcohols were analyzed with a liquid GC instrument (Shimadzu 2010 plus). The gas products were analyzed by online gas chromatography (GC, Agilent 7890A) every 17 min.  $\text{CO}$ ,  $\text{H}_2$ , and hydrocarbons were separated by different columns (molecular sieve 13X, HayeSep Q, and Carboxen-1010 PLOT) and quantified by a thermal conductivity detector (TCD) and flame ionization detector (FID). Carboxylates (formate and acetate) formed during electrolysis were analyzed by high-performance liquid chromatography (HPLC, Shimadzu Prominence), equipped with a NUCLEOGEL SUGAR 810 column and refractive index detector (RID). Alcohols were analyzed with a liquid GC instrument (Shimadzu 2010 plus), equipped with a fused silica capillary column and FID. An aliquot of the electrolyte after reaction was directly injected into the HPLC and liquid GC without further treatment. The reported Faradaic efficiency (FE) and production rate were calculated on the basis of the product distribution and current after 1 h of  $\text{CO}_2$  electroreduction at constant potentials.

**4.7. Theoretical Calculations.** Density functional theory was used to examine the specific adsorption of Li, Na, K, and Cs onto Cu(111), Cu(100), and Cu(211) in the absence and presence of near-surface water. The formation of key  $\text{CO}_2$  electroreduction intermediates, including  $\text{CO}^*$ ,  $\text{OCCO}^*$ , and  $\text{OCCOH}^*$ , was considered on the Cu(100) surface in the absence and presence of coadsorbed alkali-metal cations. We also considered the effect on Cu(100) of subsurface oxygen and surface reconstruction on alkali-metal cation adsorption and  $\text{CO}_2$  electroreduction intermediate formation. Coadsorption of iodide with the alkali-metal cations was also examined. The DFT simulations were performed using the Vienna ab initio simulations package (VASP)<sup>62–64</sup> with a plane wave basis set, the PW91 exchange and correlation functional,<sup>65</sup> and the projector augmented wave<sup>66,67</sup> method used to model the core potentials. Calculations were performed in a  $3 \times 3$  or  $2 \times 2$  unit cell, with a  $5 \times 5 \times 1$  or  $7 \times 7 \times 1$  Monkhorst–Pack mesh,<sup>68</sup> respectively, used to sample  $k$  space. A 450 eV cutoff energy was used for the plane wave basis set, and the structural optimization was performed until the forces on the atoms were less than  $0.02 \text{ eV } \text{\AA}^{-1}$ . Dipole corrections<sup>69</sup> were included in the surface normal direction (IDIPOL = 3, LDIPOL = TRUE). Each surface was comprised of four layers of Cu metal atoms, with the bottom two layers frozen at the experimentally measured lattice constant for Cu ( $3.6 \text{ \AA}$ ). Adsorption was modeled at  $1/9$  ML coverage in the  $3 \times 3$  unit cell or  $1/4$  ML in the  $2 \times 2$  unit cell (unless otherwise noted). To examine the

effects of subsurface oxygen and surface reconstruction, the most favorable subsurface oxygen absorption sites and missing row reconstructions of Cu(100) generated by oxygen adsorption were taken from Duan et al.<sup>55</sup> The “DV” missing row structure was replicated in a  $2 \times 2$  Cu(100) unit cell. The equilibrium adsorption potentials of the alkali-metal cations and of iodide were calculated following the methods we have described previously.<sup>47,70,71</sup> The reaction energies in the absence and presence of the coadsorbed alkali-metal cations for the formation of  $\text{CO}^*$ ,  $\text{OCCO}^*$ , and  $\text{OCCOH}^*$  were calculated using DFT energies at 0 K and the computational hydrogen electrode approach, as described previously.<sup>47</sup>

## ■ ASSOCIATED CONTENT

### Supporting Information

The Supporting Information is available free of charge on the ACS Publications website at DOI: 10.1021/acscatal.8b02587.

Calculations of FE and partial current density, additional SEM images, EDX analysis, XPS data, additional analysis of the electrochemical data, roughness factor measurements, and additional theoretical data (PDF)

## ■ AUTHOR INFORMATION

### Corresponding Authors

\*E-mail for M.J.J.: [mjanik@engr.psu.edu](mailto:mjanik@engr.psu.edu).

\*E-mail for B.R.C.: [roldan@fhi-berlin.mpg.de](mailto:roldan@fhi-berlin.mpg.de).

### ORCID

Dunfeng Gao: 0000-0002-2472-7349

Beatriz Roldan Cuenya: 0000-0002-8025-307X

### Notes

The authors declare no competing financial interest.

## ■ ACKNOWLEDGMENTS

This work was supported by the German Federal Ministry of Education and Research (Bundesministerium für Bildung und Forschung, BMBF) under grants #03SF0523C-“CO2EKAT” and #033RCOO4D-“e-Ethylene”, and the Cluster of Excellence RESOLV at RUB (EXC 1069) funded by the Deutsche Forschungsgemeinschaft (DFG), as well as the European Research Council (ERC-725915, OPERANDO-CAT). Financial support from the U.S. National Science Foundation (NRT-1449785) and the U.S. Department of Energy (DE-FG02-13ER16381) is also greatly appreciated. This work used the Extreme Science and Engineering Discovery Environment (XSEDE) supported by the U.S. National Science Foundation (ACI-1053575).

## ■ REFERENCES

- (1) Whipple, D. T.; Kenis, P. J. A. Prospects of  $\text{CO}_2$  Utilization via Direct Heterogeneous Electrochemical Reduction. *J. Phys. Chem. Lett.* **2010**, *1*, 3451–3458.
- (2) Montoya, J. H.; Seitz, L. C.; Chakthranont, P.; Vojvodic, A.; Jaramillo, T. F.; Nørskov, J. K. Materials for Solar Fuels and Chemicals. *Nat. Mater.* **2017**, *16*, 70–81.
- (3) Haas, T.; Krause, R.; Weber, R.; Demler, M.; Schmid, G. Technical Photosynthesis Involving  $\text{CO}_2$  Electrolysis and Fermentation. *Nat. Catal.* **2018**, *1*, 32–39.
- (4) Gattrell, M.; Gupta, N.; Co, A. A Review of the Aqueous Electrochemical Reduction of  $\text{CO}_2$  to Hydrocarbons at Copper. *J. Electroanal. Chem.* **2006**, *594*, 1–19.
- (5) Dinh, C. T.; Burdyny, T.; Kibria, G.; Seifitokaldani, A.; Gabardo, C. M.; Pelayo García De Arquer, F.; Kiani, A.; Edwards, J. P.; De Luna, P.; Bushuyev, O. S.; Zou, C.; Quintero-Bermudez, R.; Yang, Y.;

Sinton, D.; Sargent, E. H. CO<sub>2</sub> Electroreduction to Ethylene via Hydroxide-Mediated Copper Catalysis at an Abrupt Interface. *Science* **2018**, *360*, 783–787.

(6) Jiang, K.; Sandberg, R. B.; Akey, A. J.; Liu, X.; Bell, D. C.; Nørskov, J. K.; Chan, K.; Wang, H. Metal Ion Cycling of Cu Foil for Selective C–C Coupling in Electrochemical CO<sub>2</sub> Reduction. *Nat. Catal.* **2018**, *1*, 111–119.

(7) Kuhl, K. P.; Cave, E. R.; Abram, D. N.; Jaramillo, T. F. New Insights into the Electrochemical Reduction of Carbon Dioxide on Metallic Copper Surfaces. *Energy Environ. Sci.* **2012**, *5*, 7050–7059.

(8) Peterson, A. A.; Abild-Pedersen, F.; Studt, F.; Rossmeisl, J.; Nørskov, J. K. How Copper Catalyzes the Electroreduction of Carbon Dioxide into Hydrocarbon Fuels. *Energy Environ. Sci.* **2010**, *3*, 1311–1315.

(9) Larrazábal, G. O.; Martín, A. J.; Pérez-Ramírez, J. Building Blocks for High Performance in Electrocatalytic CO<sub>2</sub> Reduction: Materials, Optimization Strategies, and Device Engineering. *J. Phys. Chem. Lett.* **2017**, *8*, 3933–3944.

(10) Gao, D.; Cai, F.; Wang, G.; Bao, X. Nanostructured Heterogeneous Catalysts for Electrochemical Reduction of CO<sub>2</sub>. *Curr. Opin. Green Sustain. Chem.* **2017**, *3*, 39–44.

(11) Mistry, H.; Behafarid, F.; Reske, R.; Varela, A. S.; Strasser, P.; Roldan Cuenya, B. Tuning Catalytic Selectivity at the Mesoscale via Interparticle Interactions. *ACS Catal.* **2016**, *6*, 1075–1080.

(12) Verdager-Casadevall, A.; Li, C. W.; Johansson, T. P.; Scott, S. B.; McKeown, J. T.; Kumar, M.; Stephens, I. E. L.; Kanan, M. W.; Chorkendorff, I. Probing the Active Surface Sites for CO Reduction on Oxide-Derived Copper Electrocatalysts. *J. Am. Chem. Soc.* **2015**, *137*, 9808–9811.

(13) Mistry, H.; Varela, A. S.; Bonifacio, C. S.; Zegkinoglou, I.; Sinev, I.; Choi, Y. W.; Kisslinger, K.; Stach, E. A.; Yang, J. C.; Strasser, P.; Roldan Cuenya, B. Highly Selective Plasma-Activated Copper Catalysts for Carbon Dioxide Reduction to Ethylene. *Nat. Commun.* **2016**, *7*, 12123.

(14) Huang, Y.; Handoko, A. D.; Hirunsit, P.; Yeo, B. S. Electrochemical Reduction of CO<sub>2</sub> Using Copper Single-Crystal Surfaces: Effects of CO\* Coverage on the Selective Formation of Ethylene. *ACS Catal.* **2017**, *7*, 1749–1756.

(15) Reller, C.; Krause, R.; Volkova, E.; Schmid, B.; Neubauer, S.; Rucki, A.; Schuster, M.; Schmid, G. Selective Electroreduction of CO<sub>2</sub> toward Ethylene on Nano Dendritic Copper Catalysts at High Current Density. *Adv. Energy Mater.* **2017**, *7*, 1602114.

(16) Gao, D.; Zegkinoglou, I.; Divins, N. J.; Scholten, F.; Sinev, I.; Grosse, P.; Roldan Cuenya, B. Plasma-Activated Copper Nanocube Catalysts for Efficient Carbon Dioxide Electroreduction to Hydrocarbons and Alcohols. *ACS Nano* **2017**, *11*, 4825–4831.

(17) Kim, D.; Kley, C. S.; Li, Y.; Yang, P. Copper Nanoparticle Ensembles for Selective Electroreduction of CO<sub>2</sub> to C<sub>2</sub>–C<sub>3</sub> Products. *Proc. Natl. Acad. Sci. U. S. A.* **2017**, *114*, 10560–10565.

(18) Loiudice, A.; Lobaccaro, P.; Kamali, E. A.; Thao, T.; Huang, B. H.; Ager, J. W.; Buonsanti, R. Tailoring Copper Nanocrystals towards C<sub>2</sub> Products in Electrochemical CO<sub>2</sub> Reduction. *Angew. Chem., Int. Ed.* **2016**, *55*, 5789–5792.

(19) Grosse, P.; Gao, D.; Scholten, F.; Sinev, I.; Mistry, H.; Roldan Cuenya, B. Dynamic Changes in the Structure, Chemical State and Catalytic Selectivity of Cu Nanocubes during CO<sub>2</sub> Electroreduction: Size and Support Effects. *Angew. Chem., Int. Ed.* **2018**, *57*, 6192–6197.

(20) Dutta, A.; Rahaman, M.; Mohos, M.; Zanetti, A.; Broekmann, P. Electrochemical CO<sub>2</sub> Conversion Using Skeleton (Sponge) Type of Cu Catalysts. *ACS Catal.* **2017**, *7*, 5431–5437.

(21) Jeon, H. S.; Kunze, S.; Scholten, F.; Roldan Cuenya, B. Prism-Shaped Cu Nanocatalysts for Electrochemical CO<sub>2</sub> Reduction to Ethylene. *ACS Catal.* **2018**, *8*, 531–535.

(22) Ma, S.; Sadakiyo, M.; Heim, M.; Luo, R.; Haasch, R. T.; Gold, J. I.; Yamauchi, M.; Kenis, P. J. A. Electroreduction of CO<sub>2</sub> to Hydrocarbons Using Bimetallic Cu–Pd Catalysts with Different Mixing Patterns. *J. Am. Chem. Soc.* **2017**, *139*, 47–50.

(23) Lum, Y.; Yue, B.; Lobaccaro, P.; Bell, A. T.; Ager, J. W. Optimizing C–C Coupling on Oxide-Derived Copper Catalysts for

Electrochemical CO<sub>2</sub> Reduction. *J. Phys. Chem. C* **2017**, *121*, 14191–14203.

(24) Huang, J.; Hörmann, N.; Oveisi, E.; Loiudice, A.; De Gregorio, G. L.; Andreussi, O.; Marzari, N.; Buonsanti, R. Potential-Induced Nanoclustering of Metallic Catalysts during Electrochemical CO<sub>2</sub> Reduction. *Nat. Commun.* **2018**, *9*, 3117.

(25) Lum, Y.; Ager, J. W. Sequential Catalysis Controls Selectivity in Electrochemical CO<sub>2</sub> Reduction on Cu. *Energy Environ. Sci.* **2018**, DOI: 10.1039/C8EE01501E.

(26) Zhou, Y.; Che, F.; Liu, M.; Zou, C.; Liang, Z.; Yuan, H.; Li, J.; Wang, Z.; Luna, P.; De; Chen, P.; Blatt, E.; Quintero-Bermudez, R.; Sham, T. K.; Bals, S.; Hofkens, J.; Sinton, D.; Chen, G.; Sargent, E. H. Electron Localization Drives CO<sub>2</sub> Reduction to Multi-Carbon Hydrocarbons. *Nat. Chem.* **2018**, *10*, 974–980.

(27) Lee, S. Y.; Jung, H.; Kim, N. K.; Oh, H. S.; Min, B. K.; Hwang, Y. J. Mixed Copper States in Anodized Cu Electrocatalyst for Stable and Selective Ethylene Production from CO<sub>2</sub> Reduction. *J. Am. Chem. Soc.* **2018**, *140*, 8681–8689.

(28) Phillips, K. R.; Katayama, Y.; Hwang, J.; Shao-Horn, Y. Sulfide-Derived Copper for Electrochemical Conversion of CO<sub>2</sub> to Formic Acid. *J. Phys. Chem. Lett.* **2018**, *9*, 4407–4412.

(29) Dunwell, M.; Lu, Q.; Heyes, J. M.; Rosen, J.; Chen, J. G.; Yan, Y.; Jiao, F.; Xu, B. The Central Role of Bicarbonate in the Electrochemical Reduction of Carbon Dioxide on Gold. *J. Am. Chem. Soc.* **2017**, *139*, 3774–3783.

(30) Zhu, S.; Jiang, B.; Cai, W.; Shao, M. Direct Observation on Reaction Intermediates and the Role of Bicarbonate Anions in CO<sub>2</sub> Electrochemical Reduction Reaction on Cu Surfaces. *J. Am. Chem. Soc.* **2017**, *139*, 15664–15667.

(31) Gao, D.; Scholten, F.; Roldan Cuenya, B. Improved CO<sub>2</sub> Electroreduction Performance on Plasma-Activated Cu Catalysts via Electrolyte Design: Halide Effect. *ACS Catal.* **2017**, *7*, 5112–5120.

(32) Varela, A. S.; Ju, W.; Reier, T.; Strasser, P. Tuning the Catalytic Activity and Selectivity of Cu for CO<sub>2</sub> Electroreduction in the Presence of Halides. *ACS Catal.* **2016**, *6*, 2136–2144.

(33) Thomas, D. A.; Mucha, E.; Gewinner, S.; Schöllkopf, W.; Meijer, G.; Von Helden, G. Vibrational Spectroscopy of Fluoroformate, FCO<sub>2</sub><sup>−</sup>, Trapped in Helium Nanodroplets. *J. Phys. Chem. Lett.* **2018**, *9*, 2305–2310.

(34) Singh, M. R.; Kwon, Y.; Lum, Y.; Ager, J. W.; Bell, A. T. Hydrolysis of Electrolyte Cations Enhances the Electrochemical Reduction of CO<sub>2</sub> over Ag and Cu. *J. Am. Chem. Soc.* **2016**, *138*, 13006–13012.

(35) Pérez-Gallent, E.; Marcandalli, G.; Figueiredo, M. C.; Calle-Vallejo, F.; Koper, M. T. M. Structure- and Potential-Dependent Cation Effects on CO Reduction at Copper Single-Crystal Electrodes. *J. Am. Chem. Soc.* **2017**, *139*, 16412–16419.

(36) Resasco, J.; Chen, L. D.; Clark, E.; Tsai, C.; Hahn, C.; Jaramillo, T. F.; Chan, K.; Bell, A. T. Promoter Effects of Alkali Metal Cations on the Electrochemical Reduction of Carbon Dioxide. *J. Am. Chem. Soc.* **2017**, *139*, 11277–11287.

(37) Ayemoba, O.; Cuesta, A. Spectroscopic Evidence of Size-Dependent Buffering of Interfacial pH by Cation Hydrolysis during CO<sub>2</sub> Electroreduction. *ACS Appl. Mater. Interfaces* **2017**, *9*, 27377–27382.

(38) Jiang, Z.; Wan, W.; Lin, Z.; Xie, J.; Chen, J. G. Understanding the Role of M/Pt(111) (M = Fe, Co, Ni, Cu) Bimetallic Surfaces for Selective Hydrodeoxygenation of Furfural. *ACS Catal.* **2017**, *7*, 5758–5765.

(39) De Luna, P.; Quintero-Bermudez, R.; Dinh, C.-T.; Ross, M. B.; Bushuyev, O. S.; Todorović, P.; Regier, T.; Kelley, S. O.; Yang, P.; Sargent, E. H. Catalyst Electro-Redeposition Controls Morphology and Oxidation State for Selective Carbon Dioxide Reduction. *Nat. Catal.* **2018**, *1*, 103–110.

(40) Eilert, A.; Cavalca, F.; Roberts, F. S.; Osterwalder, J.; Liu, C.; Favaro, M.; Crumlin, E. J.; Ogasawara, H.; Friebel, D.; Pettersson, L. G. M.; Nilsson, A. Subsurface Oxygen in Oxide-Derived Copper Electrocatalysts for Carbon Dioxide Reduction. *J. Phys. Chem. Lett.* **2017**, *8*, 285–290.



- (41) Lum, Y.; Ager, J. W. Stability of Residual Oxides in Oxide-Derived Copper Catalysts for Electrochemical CO<sub>2</sub> Reduction Investigated with <sup>18</sup>O Labeling. *Angew. Chem., Int. Ed.* **2018**, *57*, 551–554.
- (42) Lee, S.; Kim, D.; Lee, J. Electrocatalytic Production of C<sub>3</sub>–C<sub>4</sub> Compounds by Conversion of CO<sub>2</sub> on a Chloride-Induced Bi-Phase Cu<sub>2</sub>O–Cu Catalyst. *Angew. Chem., Int. Ed.* **2015**, *54*, 14701–14705.
- (43) Garza, A. J.; Bell, A. T.; Head-Gordon, M. Is Subsurface Oxygen Necessary for the Electrochemical Reduction of CO<sub>2</sub> on Copper? *J. Phys. Chem. Lett.* **2018**, *9*, 601–606.
- (44) Sandberg, R. B.; Montoya, J. H.; Chan, K.; Nørskov, J. K. CO–CO Coupling on Cu Facets: Coverage, Strain and Field Effects. *Surf. Sci.* **2016**, *654*, 56–62.
- (45) Xiao, H.; Goddard, W. A.; Cheng, T.; Liu, Y. Cu Metal Embedded in Oxidized Matrix Catalyst to Promote CO<sub>2</sub> Activation and CO Dimerization for Electrochemical Reduction of CO<sub>2</sub>. *Proc. Natl. Acad. Sci. U. S. A.* **2017**, *114*, 6685–6688.
- (46) Schouten, K. J. P.; Pérez Gallent, E.; Koper, M. T. M. The Influence of pH on the Reduction of CO and CO<sub>2</sub> to Hydrocarbons on Copper Electrodes. *J. Electroanal. Chem.* **2014**, *716*, 53–57.
- (47) Akhade, S. A.; McCrum, I. T.; Janik, M. J. The Impact of Specifically Adsorbed Ions on the Copper-Catalyzed Electroreduction of CO<sub>2</sub>. *J. Electrochem. Soc.* **2016**, *163*, F477–F484.
- (48) Perez-Gallent, E.; Figueiredo, M. C.; Calle-Vallejo, F.; Koper, M. T. M. Spectroscopic Observation of a Hydrogenated CO Dimer Intermediate During CO Reduction on Cu(100) Electrodes. *Angew. Chem., Int. Ed.* **2017**, *56*, 3621–3624.
- (49) Hori, Y.; Takahashi, I.; Koga, O.; Hoshi, N. Selective Formation of C<sub>2</sub> Compounds from Electrochemical Reduction of CO<sub>2</sub> at a Series of Copper Single Crystal Electrodes. *J. Phys. Chem. B* **2002**, *106*, 15–17.
- (50) Schouten, K. J. P.; Qin, Z.; Gallent, E. P.; Koper, M. T. M. Two Pathways for the Formation of Ethylene in CO Reduction on Single-Crystal Copper Electrodes. *J. Am. Chem. Soc.* **2012**, *134*, 9864–9867.
- (51) Xiao, H.; Cheng, T.; Goddard, W. A. Atomistic Mechanisms Underlying Selectivities in C<sub>1</sub> and C<sub>2</sub> Products from Electrochemical Reduction of CO on Cu(111). *J. Am. Chem. Soc.* **2017**, *139*, 130–136.
- (52) Nie, X.; Esopi, M. R.; Janik, M. J.; Asthagiri, A. Selectivity of CO<sub>2</sub> Reduction on Copper Electrodes: The Role of the Kinetics of Elementary Steps. *Angew. Chem., Int. Ed.* **2013**, *52*, 2459–2462.
- (53) Peterson, A. A.; Nørskov, J. K. Activity Descriptors for CO<sub>2</sub> Electroreduction to Methane on Transition-Metal Catalysts. *J. Phys. Chem. Lett.* **2012**, *3*, 251–258.
- (54) Abild-Pedersen, F.; Greeley, J.; Studt, F.; Rossmeisl, J.; Munter, T. R.; Moses, P. G.; Skúlason, E.; Bligaard, T.; Nørskov, J. K. Scaling Properties of Adsorption Energies for Hydrogen-Containing Molecules on Transition-Metal Surfaces. *Phys. Rev. Lett.* **2007**, *99*, 016105.
- (55) Duan, X.; Warschkow, O.; Soon, A.; Delley, B.; Stampfl, C. Density Functional Study of Oxygen on Cu(100) and Cu(110) Surfaces. *Phys. Rev. B: Condens. Matter Mater. Phys.* **2010**, *81*, 75430.
- (56) Le Duff, C. S.; Lawrence, M. J.; Rodriguez, P. Role of the Adsorbed Oxygen Species in the Selective Electrochemical Reduction of CO<sub>2</sub> to Alcohols and Carbonyls on Copper Electrodes. *Angew. Chem., Int. Ed.* **2017**, *56*, 12919–12924.
- (57) Yang, P.; Zhao, Z.-J.; Chang, X.; Mu, R.; Zha, S.; Zhang, G.; Gong, J. The Functionality of Surface Hydroxyls on Selectivity and Activity of CO<sub>2</sub> Reduction over Cu<sub>2</sub>O in Aqueous Solutions. *Angew. Chem., Int. Ed.* **2018**, *57*, 7724–7728.
- (58) Favaro, M.; Xiao, H.; Cheng, T.; Goddard, W. A.; Yano, J.; Crumlin, E. J. Subsurface Oxide Plays a Critical Role in CO<sub>2</sub> Activation by Cu(111) Surfaces to Form Chemisorbed CO<sub>2</sub>, the First Step in Reduction of CO<sub>2</sub>. *Proc. Natl. Acad. Sci. U. S. A.* **2017**, *114*, 6706–6711.
- (59) Wu, D.; Dong, C.; Wu, D.; Fu, J.; Liu, H.; Hu, S.; Jiang, Z.; Qiao, S. Z.; Du, X. Cuprous Ions Embedded in Ceria Lattice for Selective and Stable Electrochemical Reduction of Carbon Dioxide to Ethylene. *J. Mater. Chem. A* **2018**, *6*, 9373–9377.
- (60) Biesinger, M. C.; Lau, L. W. M.; Gerson, A. R.; Smart, R. S. C. Resolving Surface Chemical States in XPS Analysis of First Row Transition Metals, Oxides and Hydroxides: Sc, Ti, V, Cu and Zn. *Appl. Surf. Sci.* **2010**, *257*, 887–898.
- (61) Wuttig, A.; Surendranath, Y. Impurity Ion Complexation Enhances Carbon Dioxide Reduction Catalysis. *ACS Catal.* **2015**, *5*, 4479–4484.
- (62) Kresse, G.; Furthmüller, J. Efficient Iterative Schemes for Ab-Initio Total-Energy Calculations Using a Plane-Wave Basis Set. *Phys. Rev. B: Condens. Matter Mater. Phys.* **1996**, *54*, 11169–11186.
- (63) Kresse, G.; Furthmüller, J. Efficiency of Ab-Initio Total Energy Calculations for Metals and Semiconductors Using a Plane-Wave Basis Set. *Comput. Mater. Sci.* **1996**, *6*, 15–50.
- (64) Kresse, G. Ab Initio Molecular Dynamics for Liquid Metals. *J. Non-Cryst. Solids* **1995**, *192–193*, 222–229.
- (65) Perdew, J. P.; Chevary, J. A.; Vosko, S. H.; Jackson, K. A.; Pederson, M. R.; Singh, D. J.;Atoms, C. F. Molecules, Solids, and Surfaces: Applications of the Generalized Gradient Approximation for Exchange and Correlation. *Phys. Rev. B: Condens. Matter Mater. Phys.* **1992**, *46*, 6671–6687.
- (66) Blöchl, P. E. Projector Augmented-Wave Method. *Phys. Rev. B: Condens. Matter Mater. Phys.* **1994**, *50*, 17953–17979.
- (67) Kresse, G.; Joubert, D. From ultrasoft pseudopotentials to the projector augmented-wave method. *Phys. Rev. B: Condens. Matter Mater. Phys.* **1999**, *59*, 1758–1775.
- (68) Monkhorst, H.; Pack, J. Special Points for Brillouin Zone Integrations. *Phys. Rev. B* **1976**, *13*, 5188–5192.
- (69) Bengtsson, L. Dipole Correction for Surface Supercell Calculations. *Phys. Rev. B: Condens. Matter Mater. Phys.* **1999**, *59*, 12301–12304.
- (70) McCrum, I. T.; Akhade, S. A.; Janik, M. J. Electrochemical Specific Adsorption of Halides on Cu 111,100, and 211: A Density Functional Theory Study. *Electrochim. Acta* **2015**, *173*, 302–309.
- (71) Mills, J. N.; McCrum, I. T.; Janik, M. J. Alkali Cation Specific Adsorption onto fcc(111) Transition Metal Electrodes. *Phys. Chem. Chem. Phys.* **2014**, *16*, 13699–13707.